Research Article

Santhoshkumar Jayakodi*, Rajeshkumar Shanmugam, Elumalai Pandian, Mani Govindasamy, Jaber M. Asiri, Krishna Kumar Yadav, and Jeong Ryeol Choi*

Controlling pore size during the synthesis of hydroxyapatite nanoparticles using CTAB by the sol–gel hydrothermal method and their biological activities

https://doi.org/10.1515/ntrev-2024-0123
received January 13, 2024; accepted October 29, 2024

Abstract: Nanorod and nanosphere hydroxyapatite (HAP) particles were synthesized by the sol–gel hydrothermal method. The size of the synthesized HAP nanoparticles was controlled using cetyltrimethylammonium bromide (CTAB) as a templating agent with molar concentrations (HAP + 0.01 M CTAB, HAP + 0.03 M CTAB, and HAP + 0.1 M CTAB). The purity, size, shape, and elemental composition of HAP were determined using powder X-ray diffraction (XRD), Fourier transform infrared spectroscopy, field emission scanning electron microscopy, and transmission electron microscopy, which enabled us to determine the nanostructure formation. Further, Brunauer–Emmett–Teller analysis of the samples proves the size of the pores to be 7–10 nm. Thus, by altering the concentration of CTAB, HAP nanorods were induced along the *c*-axis. The zeta potential values of −34.7 and −28.7 mV confirmed the stability of pure HAP and HAP + 0.01 M CTAB. Further, the biological activities of the HAP nanoparticles were determined. In the anti-microbial activity test, an increase in the inhibition with an increase in the concentration of pure HAP to 0.1 M CTAB + HAP was observed against *S. aureus*, *S. pyrogens*, *B. subtilis*, *E. aerogens*, *K. pneumoniae,* and *P. vulgaris.* About 76% of antioxidant activity was obtained from the experiments. The drug-release behavior of doxorubicin-loaded pure HAP and CTAB-coated HAP also indicates that the % of drug delivery depends on the pores, which further depends on the CTAB concentration. The cytotoxic assay also revealed potential inhibitory effects against human cancer cell lines (MCF-7), with 65% cell viability recorded at a concentration of 500 µg/ml. These findings indicate that the pore size and shape of HAP play significant roles in their biological activities.

Keywords: hydroxyapatite, CTAB, nitrogen adsorption, bactericidal, anti-oxidant, drug delivery

*** Corresponding author: Santhoshkumar Jayakodi,** Department of Biotechnology, Saveetha School of Engineering, Saveetha Institute of Medical and Technical Science (SIMATS), Chennai, 602105, TN, India, e-mail: jksanthoshk@gmail.com
*** Corresponding author: Jeong Ryeol Choi,** School of Electronic Engineering, Kyonggi University, Yeongtong-gu, Suwon, Gyeonggi-do, 16227, Republic of Korea, e-mail: choiardor@hanmail.net
Rajeshkumar Shanmugam: Nanobiomedicine Lab, Centre for Global Health Research, Saveetha Medical College and Hospital, Saveetha Institute of Medical and Technical Sciences, Chennai, 602105, Tamilnadu, India
Elumalai Pandian: Department of Chemistry, SRM Institute of Science and Technology, Ramapuram Campus, Chennai, 600089, India
Mani Govindasamy: Program in Innovative Technology of Biomedical Engineering and Medical Devices, Ming Chi University of Technology, New Taipei City, 243303, Taiwan; Research Center for Intelligence Medical Devices, Ming Chi University of Technology, New Taipei City 243303, Taiwan
Jaber M. Asiri: Department of Mechanical Engineering, College of Engineering, King Khalid University, Abha, 61421, Saudi Arabia
Krishna Kumar Yadav: Department of Environmental Science, Parul Institute of Applied Sciences, Parul University, Vadodara, Gujarat 391760, India; Environmental and Atmospheric Sciences Research Group, Scientific Research Center, Al-Ayen University, Thi-Qar, Nasiriyah, 64001, Iraq

1 Introduction

The study of living tissues and the development of life is one of the most important and complementary components of research. According to reports, millions of people experience bone defects caused by trauma, tumors, and sometimes fatal bone-related diseases [1]. Autografts and allografts have been developed to resolve these issues. Despite the advantages of such grafts, their disadvantages include a shortage of donors and morbidity. Allography results in an immune response, infections, and incompatibility [2]. Biomaterials play a vital role in these conditions

[3]. Bones are well-arrayed, naturally occurring nanocrystalline rods with lengths of 25–30 nm. It also contains collagen fibrils [4,5]. A scaffold is ideal if it mimics the replaced tissue, works in a 3D template, and supports the growth of cells that are attached naturally and function as their body part [6,7]. Hydroxyapatite (HAP) is a fascinating biomaterial for replacing hard tissues [8,9]. The synthetic component of the bone matrix shares chemical similarities with HAP ($Ca_{10}(PO_4)_6(OH)$). In addition, it is highly biocompatible with animal bones [10]. Artificial bones [11], dental [12], ocular implants, tissue engineering (scaffold matrix), and coating agents (biomedical implants) are applications of HAP [13]. HAP is a promising candidate as a delivery vehicle for proteins and drugs [8]. However, owing to the inferior mechanical properties of lab-grown HAP, its use is restricted to powders, non-load-bearing implants, and coatings [9].

Medical implants and injection devices often cause bone repair failure. One solution could be a composite material based on HAP with antibacterial properties [10,11]. Nanoparticle composites inhibit pathogenic bacteria, and a combination of HAP and the antibiotic cetyltrimethylammonium bromide (CTAB) extends antibacterial effectiveness from 2 to 4 days in human plasma [12]. The use of HAP as an alternative to antibiotics is promising because of the rising antibiotic resistance. HAP also has excellent biocompatibility and osteoconductivity, as confirmed by its *in vitro* properties [13,14].

Furthermore, bone damage and the formation of reactive oxygen species (ROSs) through chain reactions are crucial factors to consider [15]. ROSs alter the long-term integrity of bones/implants, mediate the death of osteoblasts, and stimulate osteoclastogenesis and bone resorption [16,17]. ROSs cause cell proliferation to stop, cell growth and/or development to slow, and increase cell death *via* the activation of numerous signaling pathways. ROS generation in illnesses and aging overcomes the body's antioxidant mechanisms for antioxidants (resulting in oxidative stress) [18]. Transplanted tissues can be contaminated by oxidative stress after transplantation due to disease, injury, and age [19,20]. Animals were exposed to free radicals both *in vitro* and *in vivo*, which accelerated bone resorption. Therefore, the inclusion of antioxidants such as ascorbic acid and vitamins is required. They can help accelerate the healing of bone fractures/implants (remove ROSs) and, therefore, protect against osteoporosis [21]. HAP reduced ROS levels and showed enhanced activity because of its large surface area and mechanical properties. HAP is the primary chemical constituent of the bone tissue [22,23]. It has been widely considered for drug delivery activities owing to its good biocompatibility, biodegradability, bioresorbability, osteogenesis, and low solubility. Replacement of different types of ions is required to modify the solubility of HAP [24,25]. Because HAP dissolution is pH-sensitive, drugs can be delivered to specific cancerous zones. Furthermore, recent studies have demonstrated that HAP particles have anticancer characteristics [26,27]. The antibiotics required for bone-replacement zones are well carried by HAP. Drugs may be loaded into HAP either *in situ* or *ex situ* [28]. HAP nanoparticles have frequently been employed as templates or scaffolds because of their superior bioactivity, biodegradability, and osteoconductivity.

Advancements in biomaterials have significantly impacted the fields of regenerative medicine and tissue engineering. Among the various materials, HAP and calcium titanate apatite (CTAP) have garnered considerable attention due to their promising properties for bone regeneration and implant applications.

HAP, a naturally occurring form of calcium apatite, is known for its excellent biocompatibility and osteoconductive properties. Studies have consistently demonstrated HAP's efficacy in promoting bone growth and integration with surrounding tissues. For instance, Li *et al*. explored the use of HAP coatings on titanium implants, showing enhanced osseointegration and improved mechanical stability in preclinical models [1]. Similarly, Zhang *et al*. investigated HAP-based scaffolds for bone tissue engineering and reported superior cellular proliferation and mineralization compared with non-coated scaffolds [2].

In contrast, CTAP is a new material with a structure that combines the beneficial properties of both calcium titanate and HAP. Patel *et al*. demonstrated that CTAP exhibits unique bioactivity and mechanical strength characteristics, making it a viable alternative to HAP. Their study found that CTAP not only supported better cell attachment and proliferation but also showed improved mechanical performance in comparison to traditional HAP materials [3]. Moreover, Sun *et al*. reported that CTAP scaffolds have enhanced osteogenic potential and better structural integration with bone compared to conventional HAP scaffolds, suggesting CTAP's potential for more demanding orthopedic applications [4]. Additionally, comparative studies have highlighted the distinct advantages of CTAP over HAP in certain contexts. For example, Zhou *et al*. investigated the long-term stability and bioactivity of CTAP *versus* HAP in a rabbit femur model. Their findings indicated that while both materials supported bone healing, CTAP exhibited superior resistance to dissolution and degradation, leading to more durable bone–implant interfaces [5].

Here, we describe the methods used to synthesize HAP nanorods at a reaction temperature of 160°C for 20 h by appropriately regulating the additive concentration and pH. The crystalline structure, form, size, and growth mechanism

of HAP are briefly discussed. Further, antimicrobial, antioxidant, and drug delivery studies were carried out using the synthesized HAP. To the best of our knowledge, no studies have been reported on the sol–gel mediated hydrothermal synthesis of pure and template-assisted HAP.

2 Materials and methods

Calcium nitrate tetrahydrate ($Ca(NO_3)_2{\cdot}4H_2O$) and diammonium hydrogen phosphate (DHP) ($(NH_4)_2HPO_4$), CTAB, ammonia solution, 2,2-diphenyl-1-picrylhydrazyl (DPPH), MTT (3-(4,5-dimethylthiazol-2-yl)-2,5-diphenyltetrazolium bromide), fetal bovine serum, Muller–Hinton (MH) agar, methanol, phosphate buffer solution, and doxorubicin (DOX) were purchased from Avra Synthesis Pvt. Ltd. and used without further purification. A magnetic stirrer, hot air oven, autoclave, UV-visible spectrophotometer, laminar air flow, CO_2 incubator, incubator, and rotary shaker were used for determining the biological activities.

2.1 Synthesis and characterization of HAP nanoparticles

The HAP nanostructures were synthesized using a sol–gel-mediated hydrothermal method assisted by a surfactant CTAB. $Ca(NO_3)_2{\cdot}4H_2O$ and $(NH_4)_2HPO_4$ (DHP) were dissolved separately in double-distilled Millipore water to maintain a stoichiometric ratio (Ca/P) of 1:67. The phosphate-containing solution was added to 0.01, 0.03, and 0.1 mol of CTAB as a template. The $Ca(NO_3)_2{\cdot}4H_2O$ and $(NH_4)_2{\cdot}HPO_4$ + CTAB mixture was stirred for 2 h at 70°C. Then, (DHP + CTAB) was added to $Ca(NO_3)_2{\cdot}4H_2O$ slowly and stirred continuously till a gel was formed. The resulting white gel was transferred to an autoclave made of stainless steel. The hot air oven was maintained at 160°C in a hot air oven for 20 h. The precipitate was obtained and centrifuged for 15 min at 10,000 rpm. The sediment was completely cleaned with acetone and water. To maintain the pH of the mixture at 11, ammonia solution was added continuously. The precipitate was then calcined for 5 h at 600°C after being air dried at 80°C.

X-ray diffraction (XRD) with Cu Kα radiation at a wavelength of 1.5405 Å, a voltage of 40 kV, and a current of 30 mA was used to analyze the crystalline structure. The scan rate was 0.05°/min over the range of 2θ = 5°–90° (XRD D8 Advance BRUKER). A Fourier transform infrared (FTIR) spectrophotometer (Shimadzu 43000, Shimadzu, Japan) was used to perform the functional group analysis utilizing the KBr disk method. The wavelength was chosen to be 4,000–400 cm^{-1} with a resolution of 2 cm^{-1}. Field emission scanning electron microscopy (FESEM) images were recorded using a Zeiss FE-SEM SUPRA 55 instrument. The voltage was maintained at 5 kV. The dynamics of HAP were ascertained, and the zeta potential was calculated using an SZ100 particle size analyzer (Horiba Scientific SZ-100).

2.2 Antimicrobial activity

The well diffusion method was used to examine the antibacterial efficacy of synthetically produced pure HAP, 0.01 M CTAB + HAP, 0.03 M CTAB + HAP, and 0.1 M CTAB + HAP against Gram-positive (*B. subtilis* and *S. aureus*) and Gram-negative (*K. pneumoniae* and *E. coli*) strains of bacteria. Bacterial cultures were isolated and identified in the Department of Microbiology at the Saveetha Institute of Medical and Technical Sciences in Chennai. Using sterilized cotton swabs, different bacterial strains were dispersed in MH agar. A cork borer was used to drill the wells, and a 30 µg/ml sample was added. Chloramphenicol served as a positive control. The inhibited zone (mm) was measured following a 24-h incubation period at 37°C [29].

2.3 Antioxidant activity

The antioxidant activity of HAP was assessed using a DPPH (2,2-diphenyl-1-picrylhydrazyl) radical scavenging assay. Pure HAP, HAP + 0.01M CTAB, HAP + 0.03M CTAB, and HAP + 0.1M CTAB at concentrations of 10–50 µg/ml were mixed with 500 µl of 0.01 mM DPPH solution and diluted to 3 ml with methanol. The mixture was thoroughly mixed and left in the dark for 30 min. The absorbance of the solution was measured using a UV-visible spectrophotometer calibrated to 517 nm, with ascorbic acid as the standard. The percentage of activity related to radical scavenging (RSA) was calculated using the following formula (equation (1)) [30]:

$$\% \text{ RSA } ¼ \text{ Absorbance of blank } /\text{Absorbance of sample Absorbance of blank} \times 100. \quad (1)$$

2.4 Drug delivery

In an ethanol solution, 20 mg of pure HAP, HAP + 0.01 M CTAB, HAP + 0.03 M CTAB, and HAP + 0.1 M CTAB are dispersed in 10 ml of the drug (DOX). For 24 h, a magnetic stirrer was used to stir the solution. Drug molecules for DOX adsorbed onto the HAP surface. The drug-loaded HAP, HAP + 0.01 M CTAB, HAP + 0.03 M CTAB, and HAP

+ 0.1 M CTAB were centrifuged for 15 min at 3,000 rpm. The DOX concentration was determined using UV-Vis spectroscopy. After measuring the absorbance spectrum of the unloaded drug and the UV-Vis peak of DOX absorption, the drug-loaded HAP was then recovered after centrifugation. The percentage of DOX drug-loaded HAP was calculated using equation (2) [31]:

$$\text{Drug loading capacity} = \frac{\text{Total amount of drug} - \text{Free drug}}{\text{HAP weight}} \times 100. \quad (2)$$

2.5 Anticancer activity

The synthesized HAP were tested for their anticancer activity against MCF7 cancer cell lines. About 1×10^{-2} cells per well were cultured for 1 day. The cells were then rinsed with 100 µl of serum-free medium and starved for 1 h in a CO_2 incubator at 37°C. HAP (25–500 µg/ml) was applied to the cells and incubated for 1.5 days. DMSO was used as the negative control. After 36 h, 20 µl of MTT solution was added to each 96 well and incubated for 4 h. Finally, DMSO (200 µl) was added, and the absorbance was measured at 57 nm using an ELISA reader.

2.6 Release studies

The drug release of DOX from pure HAP, HAP + 0.01 M CTAB, HAP + 0.03 M CTAB, and HAP + 0.1 M CTAB was studied. About 1, 5, and 10 mg of HAP loaded with drugs were added to 10 ml of phosphate buffer solution (pH 7.4). This solution was shaken (120 rpm) at 37°C for 48 h. At different time intervals, 3 ml of supernatant was removed, and the release ability of the DOX was tested using a UV-Vis spectrophotometer. The release of DOX was evaluated using equation (3):

$$\text{Drug release} = 1 - \frac{\text{Absorbance } (t)}{\text{Aborbance } (t_0)} \times 100, \quad (3)$$

where t_0 is the drug absorbance at the initial time, and t is the drug absorbance at regular time intervals.

3 Results and discussion

3.1 XRD analysis of the synthesized HAP

The XRD diffraction peaks shown in Figure 1 indicate the crystalline nature of the pure and CTAB-mediated HAP. The XRD peaks are indexed to the (0 0 2), (2 1 0), (2 1 1), (3 0 0), (2 0 2), (2 1 2), (4 0 1), (2 1 3), (0 0 4), (3 0 4), and (5 1 3) planes and are 25.36°, 28.62°, 31.53°, 32.77°, 33.79°, 39.40°, 46.43°, 52.92°, 63.67°, and 77.50°, respectively. This demonstrates that the obtained samples are of the pure form of hexagonally structured HAP. The results from HAP and the standard data set are highly dependable, with framework dimensions of $a = b = 0.9414$ nm, $c = 0.6879$ nm (space group P63/m). No peaks of any other secondary-phase intermediate compounds like $CaHPO_4{\cdot}2H_2O$ or $Ca_2(HPO_4)_2(PO_4)_4{\cdot}5H_2O$ were observed, indicating that the reaction output is 100% phase-pure HAP [32]. The diffraction peaks are indexed as pure HAP with a space group of *P*63/m, as claimed by JCPDS #73-0293 [33]. The researcher also recounted the XRD pattern, indicating that the inorganic phase of the sample is HAP [4,34].

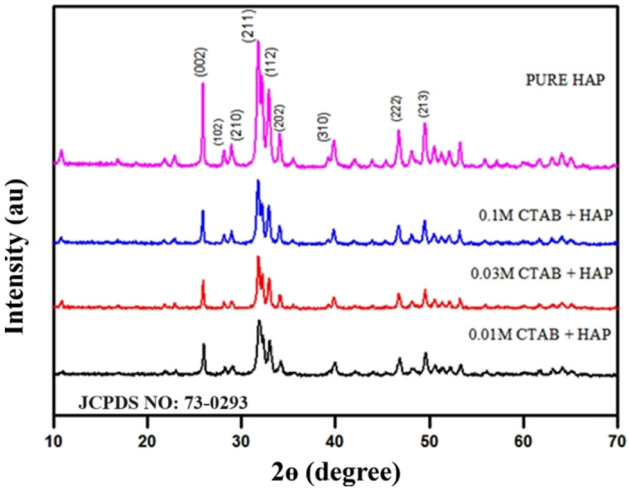

Figure 1: XRD analysis of the synthesized HAP.

Scherrer's formula (equation (4)) was used to determine the HAP crystallite size:

$$D_{hkl} = \frac{0.92\lambda}{\beta \cos \theta}, \quad (4)$$

where D_{hkl} is the average crystallite size of HAP, Cu Kα, XRD wavelength is 1.5405 Å, its full width at half-maximum intensity (FWHM), and half of its Bragg's angle are each given in units. The average crystallite sizes of the nanostructured HAP samples generated are 31, 116, 83, and 87 nm, respectively, for the phases of pure HAP, HAP + 0.01 M CTAB, HAP + 0.03 M CTAB, and HAP + 0.1 M CTAB, respectively. The lattice properties of HAP did not change noticeably ($a = b = 9.4824$ and $c = 6.8927$).

3.2 FTIR analysis

FTIR analysis establishes the functional groups of the generated HAP microstructures, as shown in Figure 2. The

peak at 1,377 cm^{-1} is due to carbonate ions in the HAP particles that arrived from atmospheric CO_2 at the time of analysis [35]. The peak between 2,170 and 3,810 cm^{-1} is due to water adsorption on HAP [36,37], and the absorption peak at 1,631 cm^{-1} was attributed to the bending mode of H_2O [38,39]. The sharp peak intensities at 1,050 and 565 cm^{-1} are caused by the stretching modes of PO_4^{3-} and the bending modes of the apatite structure [33,40]. The lack of additional peaks in the FTIR spectrum indicates that HAP is purified. The FTIR results indicate the absence of surfactant molecules in HAP.

3.3 FESEM analysis of the synthesized HAP

The succession of uniform nanospheres to nanorods at different concentrations of CTAB is shown in Figure 3. The FESEM analysis of the sample shows the formation and size modification of HAP by CTAB.

In the absence of CTAB, spherical particles are formed. However, upon adding CTAB at different concentrations, the shape of the particles changes from spherical to rod-shaped, which purely depends on the concentration of CTAB [33]. The FESEM images reveal numerous related pores, further demonstrating the effect of CTAB on HAP in regulating the particle size and shape [41]. The Ca/P ratios are found to be 1.67, 1.56, 1.54, and 1.55 for pure HAP, HAP + 0.01 M CTAB, HAP + 0.03 M CTAB, and HAP + 0.1 M CTAB, respectively (Figure 4). The reduction in Ca/P ratios may be attributed to the presence of pores.

Vinayagam *et al.* reported that the surface morphology of *Muntingia calabura* leaf extract-mediated HAP NPs showed irregular rod-like structures, typical of HAP NPs from eggshells. Intense agglomeration likely results from interactions between *Muntingia calabura* phytochemicals and HAP NPs. A rough, non-uniform surface increases the surface area and enhances biomedical suitability [42].

3.4 Transmission electron microscopy (TEM) analysis of HAP and 0.1 M CTAB + HAP

The SEM results suggest that the CTAB morphology transformation may be the most important parameter in determining the HAP microstructure. To analyze the morphology, TEM was performed (HAP and 0.1 M CTAB + HAP (Figure 5a and b)). In pure HAP, some dispersively agglomerated particles were found, and the size range is 20–100 nm. TEM analysis revealed that the particles are nanosized and have a spheroid form in 0.1 M CTAB + HAP. Furthermore, the TEM image highlighted the nanocomposite spheroid morphology with a nanometric particle size. A spheroid particle forms when particles collide along their long axis or parallel to their plane due to their high surface energy. The TEM findings are consistent with the SEM results.

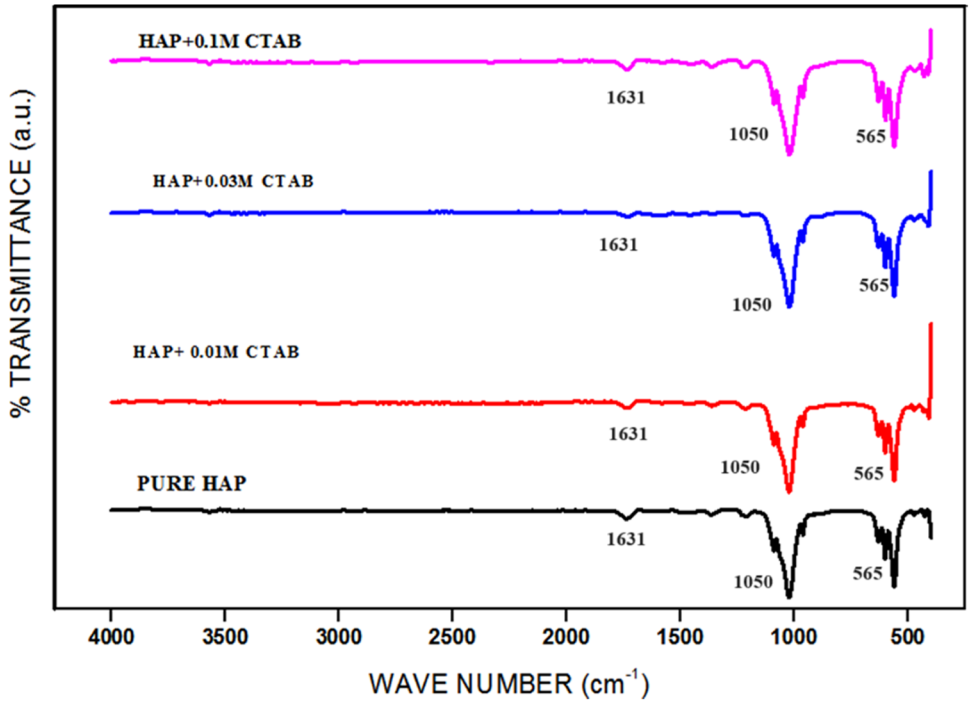

Figure 2: FTIR analysis of the synthesized HAP.

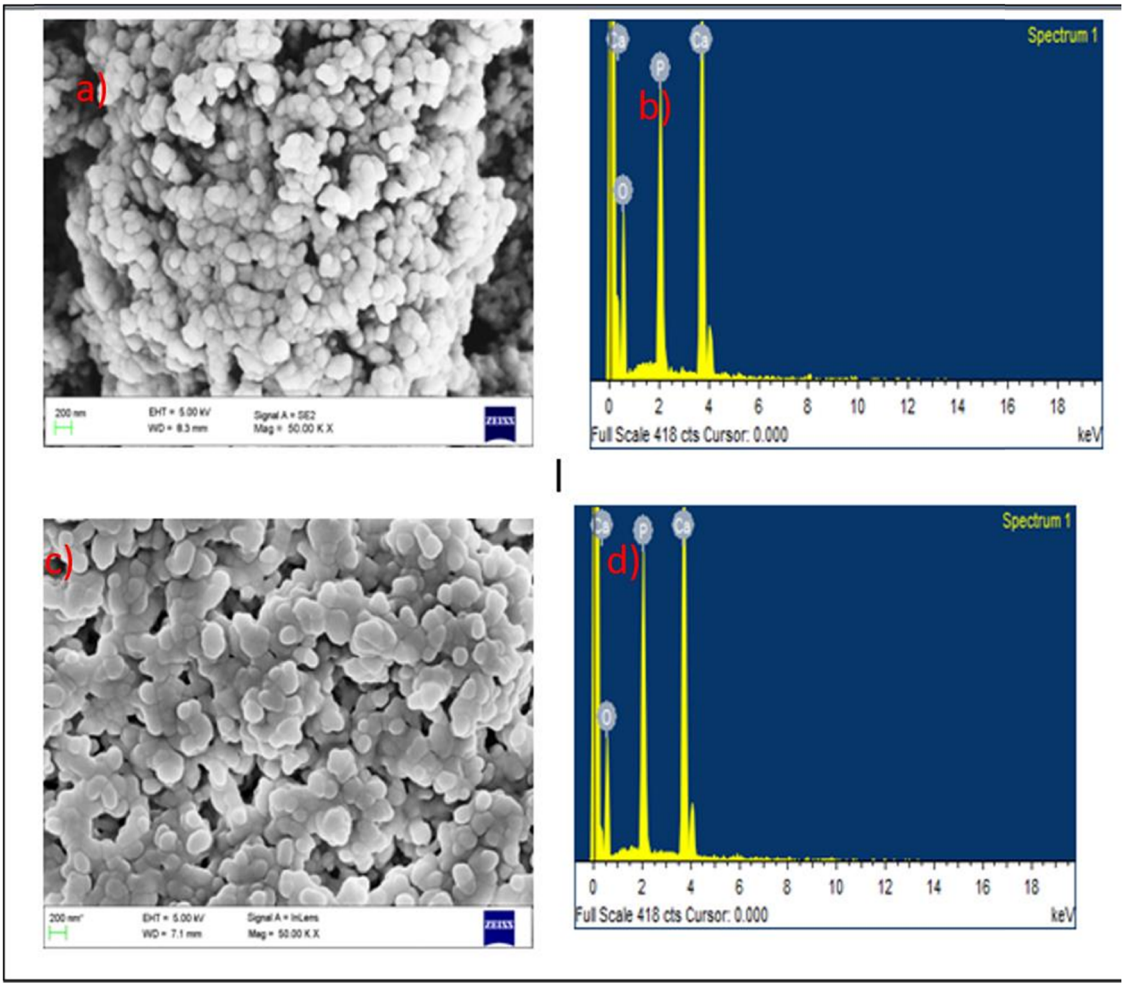

Figure 3: FESEM-EDAX analysis of the synthesized pure HAP (a and b) and 0.1 M CTAB + HAP (c and d).

Sánchez-Campos *et al.* examined the effects of the cationic surfactant CTAB on the morphology and particle size of HAP using the microwave method with constant pH, time, and temperature. TEM revealed that the surfactant significantly reduced the size of HAP, producing nanorods with an average diameter of 43.17 nm and a length of 136.52 nm when 0.45 wt% surfactant was used [43].

The effectiveness of hydrothermal and microwave techniques, both with and without ethylenediaminetetraacetic acid (EDTA) and CTAB surfactants, was systematically examined under similar conditions to produce mesoporous nanorod-like HAP particles, as reported by Singh *et al.* [44].

3.5 Zeta potential analysis

A zeta potential analysis of the HAP is performed to determine its stability. The zeta potential values are listed in Table 1. This study also confirmed that CTAB-HAP is more stable than pure HAP. This demonstrates that these materials are suitable for drug delivery. According to previous studies [45,46], if the zeta potential is negative, the specimen is suitable as an implant, which can grow along with live or viable cells. A negative zeta potential influences Ca^{2+} ions to participate in cell adhesion by depositing cells in an extracellular matrix. Zhu *et al.* reported the optimal HAP nanoparticle agglomerate size and emulsion stability; it is recommended to use a CTAB concentration of 8 mM when fabricating HAP nanoparticle-stabilized emulsion [47].

3.6 Brunauer–Emmett–Teller (BET) analysis of the synthesized HAP

The BET analyses of the above samples are carried out, and the results are shown in Table 2. The pore size of the samples decreased when CTAB was used. These results, which are based on calculations, show the ability of the surfactant

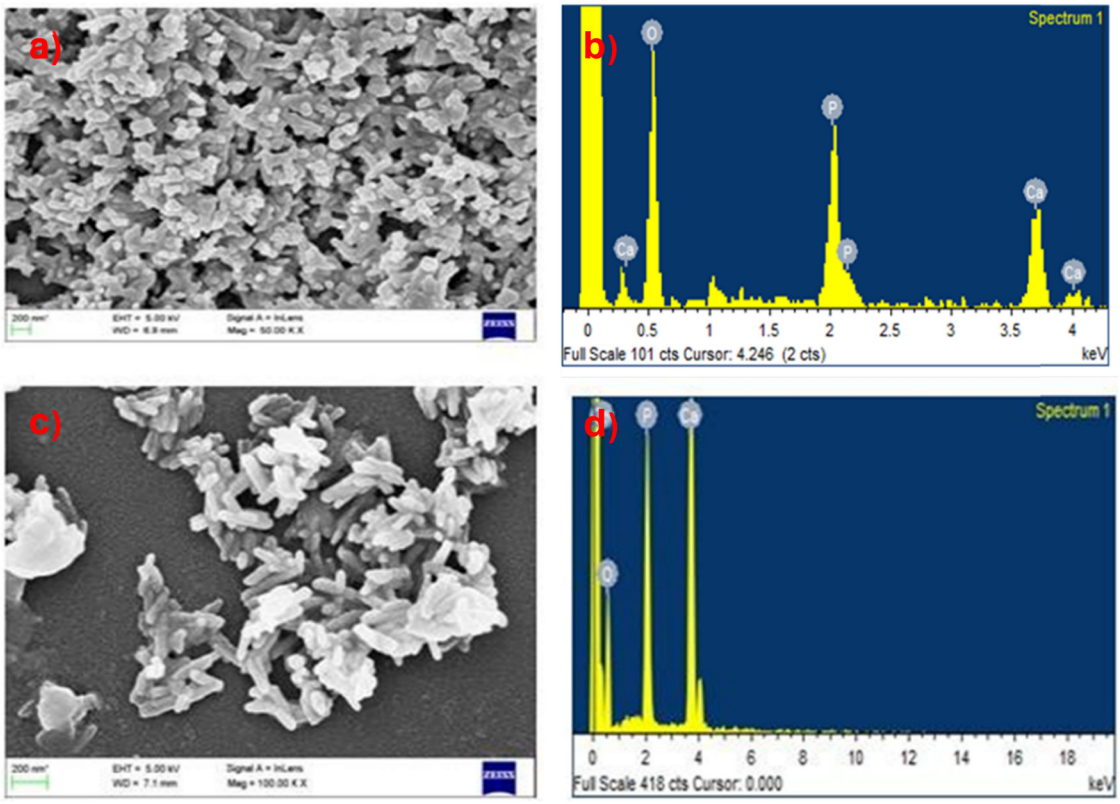

Figure 4: FESEM-EDAX analysis of 0.3 M CTAB + HAP (a) FESEM and (b) EDAX and 0.1 M CTAB + HAP (c) FESEM and (d) EDAX.

to change its structural properties and thereby create pores. The organic CTAB and ammonium salt decompose during calcination, followed by the formation of many irregular pores, which agrees with the results of Yan *et al.* [48]. The pore size, which ranges from 6 to 1 nm, makes this material suitable for biological and piezoelectric applications [38]. The synthesis method also plays a crucial role in pore formation. The nitrogen adsorption–desorption isotherm analysis (Figure 6) proves the presence of many open-ended pores and also confirms the mesoporosity of the material. Nitrogen is frequently used to perform BET analysis. Table 2 clearly shows that when the pore volume in the sample decreased, so did the pore diameter. In comparison, HAP + 0.03 M CTAB has an enhanced

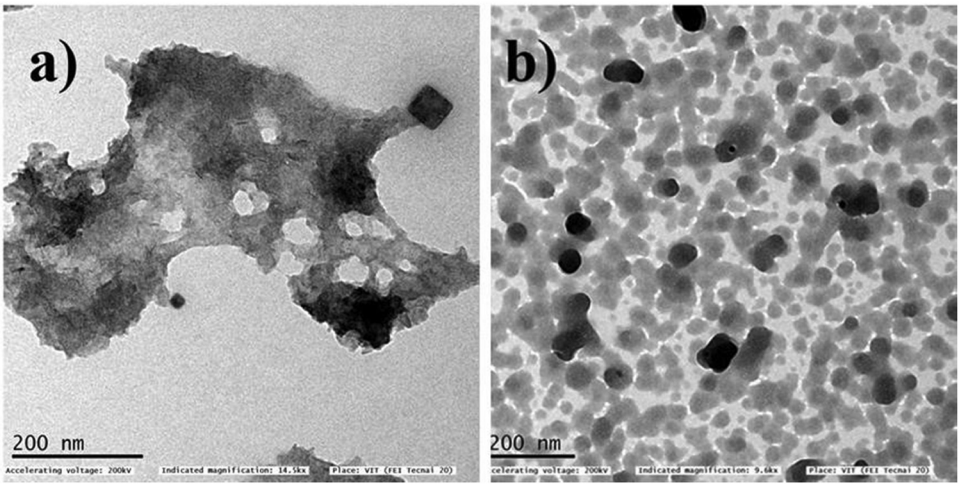

Figure 5: TEM analysis of (a) HAP and (b) 0.1 M CTAB + HAP.

Table 1: Zeta potential analysis of the synthesized HAP

S. no	Material with concentration	Zeta potential (mV)
1	PURE HAP	−34.7
2	HAP+ CTAB 0.01 M	−31.8
3	HAP+ CTAB 0.03 M	−34.0
4	HAP+ CTAB 0.10 M	−28.9

average pore diameter, indicating that this sample has better biological activity than the other HAPs.

3.7 Antimicrobial activity

The level of susceptibility shows a contrasting variation in the antibacterial assay between the Gram-positive and Gram-negative bacterial strain (Figure 7) using HAP and CTAB template HAP, which was established by the zone of inhibition. *S. aureus* shows the highest susceptibility to Gram-positive strains (HAP + 0.1 M CTAB) (18 ± 0.54 mm). The inhibitory impact was shown to be very low against *B. subtilis* (9 ± 10 mm) and medium for *S. pyrogens* (HAP + 0.1 M CTAB), respectively. The inhibitory impact was shown to be very low against *B. subtilis* (9 ± 1.0 mm) and medium for *S. pyrogens* (HAP + 0.1 M CTAB), respectively. In contrast to Gram-negative bacteria, the action of HAP (HAP + 0.1 M CTAB) also revealed notable variability in the levels of inhibition. Maximum inhibition was observed against *E. aerogenes* (19 ± 0.5 mm); however, *K. pneumoniae* activity was reduced (8 ± 1 mm), and *P. vulgaris* showed only a very weak inhibitory effect (6 ± 0.2 mm). Additionally, it was noted that both the CTAB + HAP surface area and particle size significantly influenced the antibacterial activity.

This may explain the improved inhibition exhibited by 0.1 M CTAB + HAP toward the bacterial pathogens. It has been demonstrated that CTAB + HAP has a strong inhibitory effect on bacterial pathogens. Unexpectedly, a recent study confirmed our assertion that synthetic HAP has strong bactericidal effects against Gram-negative bacteria [40]. The zone of inhibition efficacy differs between Gram-positive and Gram-negative bacterial strains due to the differences

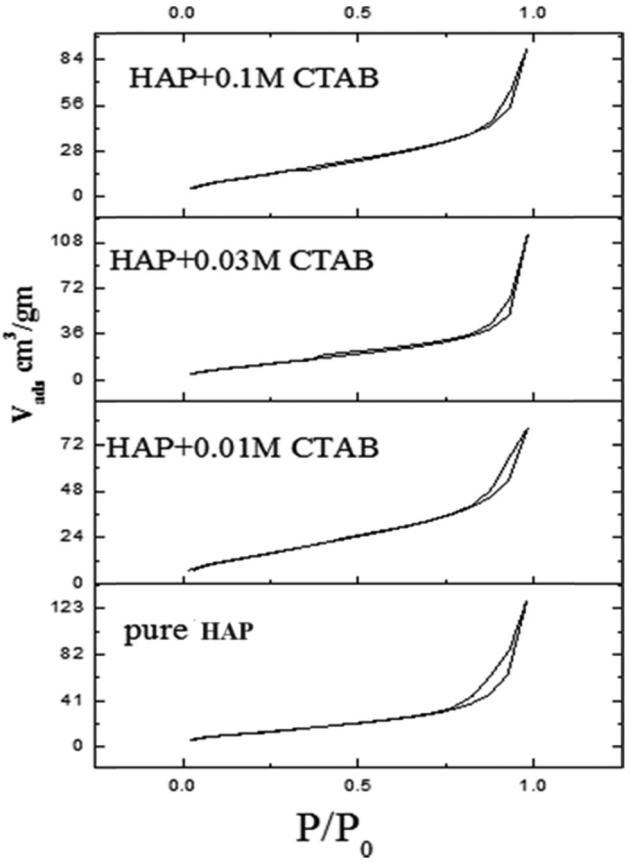

Figure 6: Nitrogen absorption measurements of the synthesized HAP.

in the cell membrane components between the two types of bacteria, which alter the HAP adsorption process. A large number of holes and a high level of negative charge on the surface of the cell wall cause HAP to be more attracted to it, resulting in cell membrane breakdown and death in Gram-positive bacterial strains. The mechanism of the antibacterial activity is shown in Figure 8 [49].

3.8 Mechanism of antibacterial activity of HAP

CTAB+HAP act as an antimicrobial agent through the following mechanisms: The combination of CTAB and HAP

Table 2: BET analysis of the synthesized HAP

Sample	Surface area (m^2/g)	Total pore volume (cm^3/g)	Average pore diameter (nm)
PURE HAP	48.37	0.132	10.95
HAP + 0.01 M CTAB	56.51	0.104	7.42
HAP + 0.03 M CTAB	47.41	0.101	8.52
HAP + 0.1 M CTAB	51.80	0.101	7.83

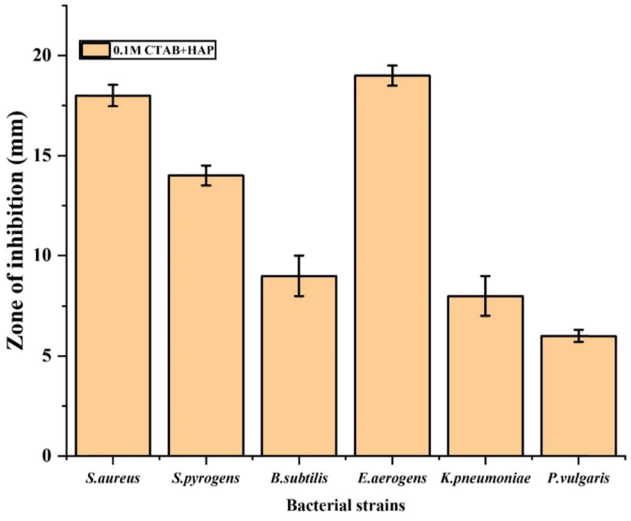

Figure 7: Antibacterial activity of HAP + 0.1 M CTAB.

exhibits potent antibacterial effects *via* multiple mechanisms. First, the production of ROS in bacterial cells induces oxidative stress, leading to significant damage to cellular components such as lipids, proteins, and DNA. This oxidative damage can cause mutations and, in severe cases, cell death. Second, the breakdown of CTAB and HAP releases calcium ions (Ca^{2+}), which disrupt key cellular processes, including enzyme activity, amino acid metabolism, and protein synthesis [50]. This disruption interferes with bacterial metabolism, leading to cell dysfunction and eventual mortality. Third, the interaction of HAP and CTAB with the bacterial cell membrane through electrostatic forces causes physical damage to the membrane, resulting in the leakage of intracellular contents and the collapse of cellular integrity. The combined action of ROS production, calcium ion release, and membrane disruption makes the CTAB + HAP combination highly effective in killing bacterial cells [51].

3.9 Antioxidant activity

The dose-dependent antioxidant effects of the HAP and CTAB + HAP against DPPH free radicals were investigated (Figure 9). At a high concentration (50 µg/ml) of HAP and CTAB + HAP, maximum radical inhibition (71%) was observed. In comparison with synthetic HAP and CTAB + HAP, ascorbic acid displayed a minimal inhibitory effect (64%) at a dose of 50 g/ml. In agreement with the above work, our investigation showed the highest inhibition rate of DPPH activity. Based on the results, it was confirmed that the porous substance CTAB + HAP was essential for creating the DPPH radical scavenging activity.

3.10 Mechanism of DPPH and HAP + CTAB

Antioxidants are compounds that delay or prevent oxidative damage to target molecules. The distinctive feature of an antioxidant is its capacity to remove free radicals due to

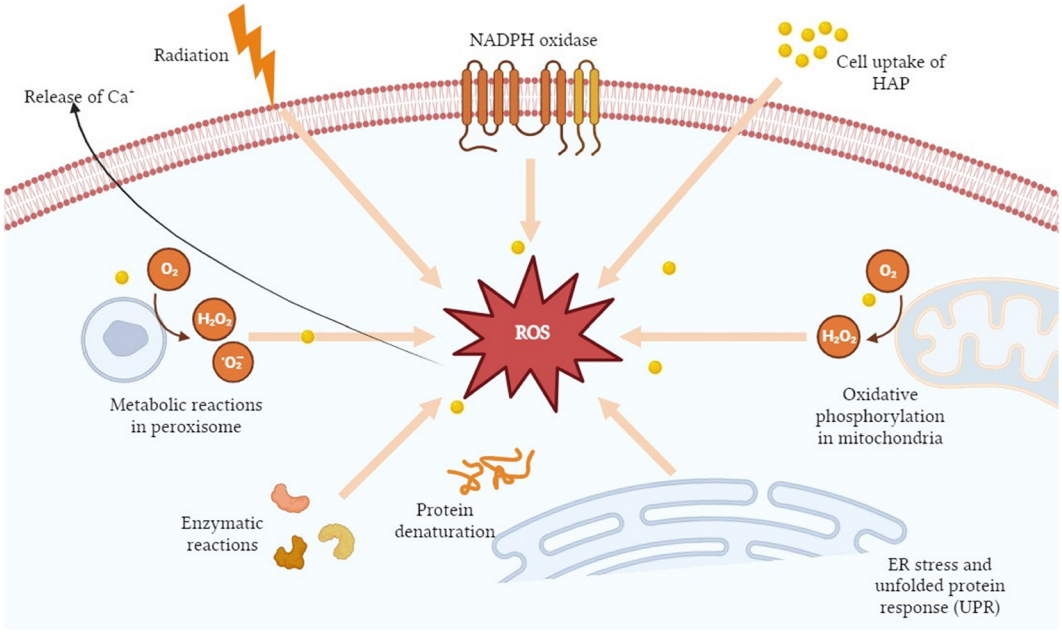

Figure 8: Schematic representation of the antibacterial mechanism of HAP and CTAB against bacterial organisms.

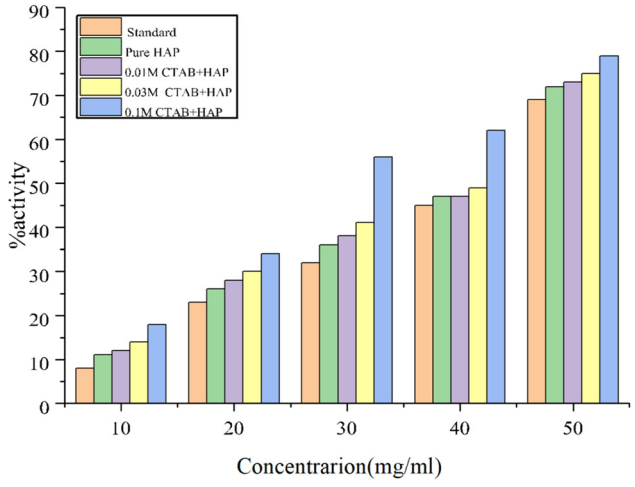

Figure 9: Antioxidant activity of HAP.

the presence of redox hydrogen donors and singlet oxygen quenchers [52]. Free radicals can be removed by both natural (plant/microbial/animal-based chemicals) and synthetic (butylated hydroxyl anisol tetrabutylhydroquinine and butylated hydroxyl toluene) antioxidants [53]. However, natural antioxidants are preferred because they are considered comparatively safer and are known to cause fewer side effects [41].

The DPPH test is a quick, reliable, and affordable method for assessing antioxidant activity. Stable diamagnetic molecules that form stable free radicals, such as DPPH, must accept an electron or hydrogen radical [54]. Compared to other procedures, the DPPH radical method is a popular method to assess antioxidant activity. The mechanism of DPPH activity is displayed in Figure 10.

3.11 Drug delivery

The drug release of DOX from pure HAP, 0.01 M CTAB + HAP, 0.03 M CTAB + HAP, and 0.1 M CTAB + HAP is shown

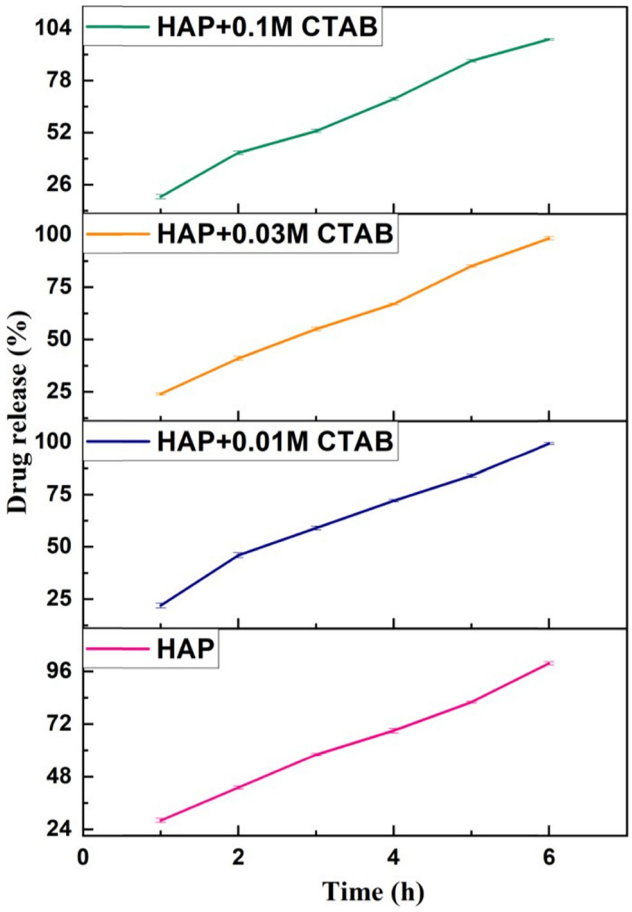

Figure 11: Drug release of HAP and CTAB-coated HAP (10 mg).

in Figure 12. When 10 mg of pure 0.01 M CTAB + HAP, 0.03 M CTAB + HAP, or 0.1 M CTAB + HAP were utilized, approximately 69% of the DOX was released after 1 h. Within 6 h, 99, 97, 96, and 98.9% of DOX were released from the HAP. A burst release was seen when 10 mg of pure HAP, HAP + 0.01 M CTAB, HAP + 0.03 M CTAB, and HAP + 0.1 M CTAB were used, indicating that the release was absorbed in the shallow nanochannels (Figure 11).

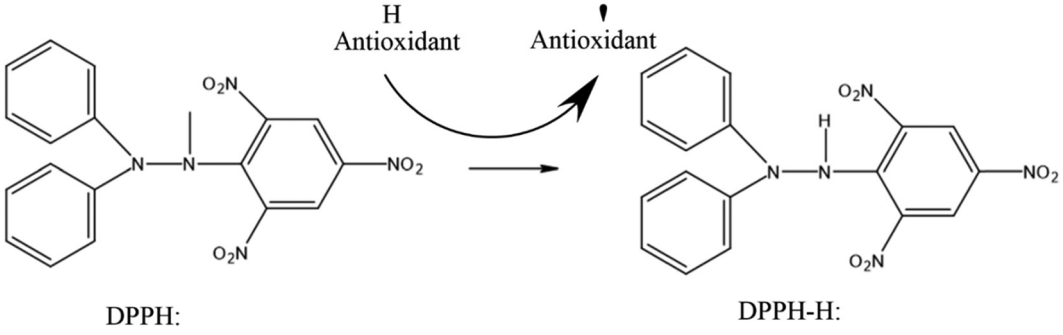

Figure 10: Antioxidant activity of HAP.

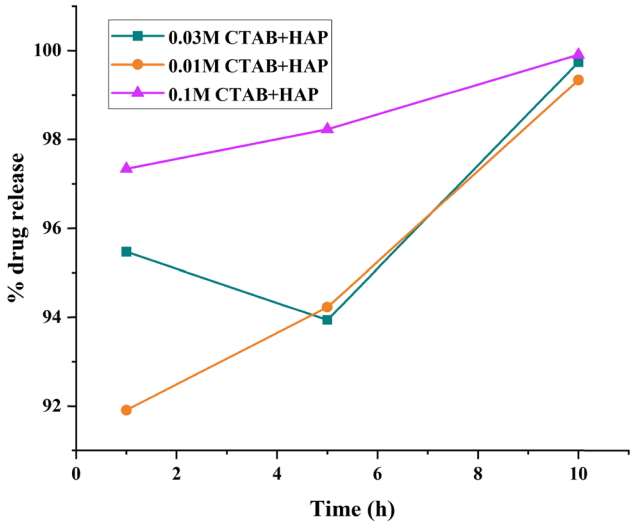

Figure 12: % drug release of HAP at various concentrations.

Doxorubicin was slowly released using 5 and 1 mg of pure HAP, HAP + 0.01 M CTAB, HAP + 0.03 M CTAB, and HAP+ 0.1 M CTAB (Figure 12).

Under neutral conditions, a low release rate supports sustained release, minimizes drug loss, and alleviates adverse effects. The amount of HAP was reduced due to chemical adsorption and the quantity of DOX drug released. At a later stage, DOX molecules may hydrogen bind to the surface of HAP and release it relatively slowly [55]. HAP has a high loading capacity and gradual drug delivery due to its high specific area and the hydrogen bonds that they form with DOX [56].

3.12 Anticancer activity

The cytotoxic effect of the HAP on MCF-7 cell lines was studied using the MTT assay. The effects observed at various concentrations (25–500 µg/ml) were dose-dependent (Figure 13). The maximum cell growth inhibition (65%) was recorded at 500 µg/ml after 36 h. Microscopic visualization of HAP-treated cell lines showed distinct morphological features, such as cell shrinkage with condensed cytoplasm and fragmented nuclei, confirming the induction of apoptosis. The improved cytotoxic effect of HAP is attributed to the combination of CTAB and HAP. Camptothecin, used as a control, showed 49% cell inhibition at the maximum concentration (500 µg/ml) tested in this study. The mechanism of the cytotoxic effect of HAP was due to the physicochemical interactions of HAP with the functional groups of nitrogen bases, cellular proteins, and phosphate groups of the genetic material (DNA). Based on several studies investigating cytotoxicity against different tumor cell lines, we found that HAP showed remarkable biological activities. Sánchez-Campos *et al.* suggested the use of surfactants, especially in HAP, for efficiently producing smaller particles and enhancing the synthesis process in biomaterials research [43]. Furthermore, HAP-CTAB nanocomposites were found to be non-cytotoxic, whereas lead-contaminated solutions exhibited high toxicity against HeLa cells, with the degree of toxicity being strongly correlated with the concentration of lead ions [57].

4 Conclusion

By utilizing CTAB as the sole templating agent in a sol–gel, it is possible to successfully modify the size and form of nano-HAP particles. The production of tiny nanoscale spheres and rods was aided by a surfactant, which served as a template. The results of the FTIR and XRD tests demonstrated the development of phase-pure HAP and particle quality. TEM and FESEM analyses showed the development of spherical and rod-like HAP. BET analysis validated the 6–10 nm-sized pores that were created. These nanoparticles with customizable structures may be good coating materials for implantation and medication delivery systems with biological applications. *In vitro* antimicrobial activity tests were carried out using the well diffusion

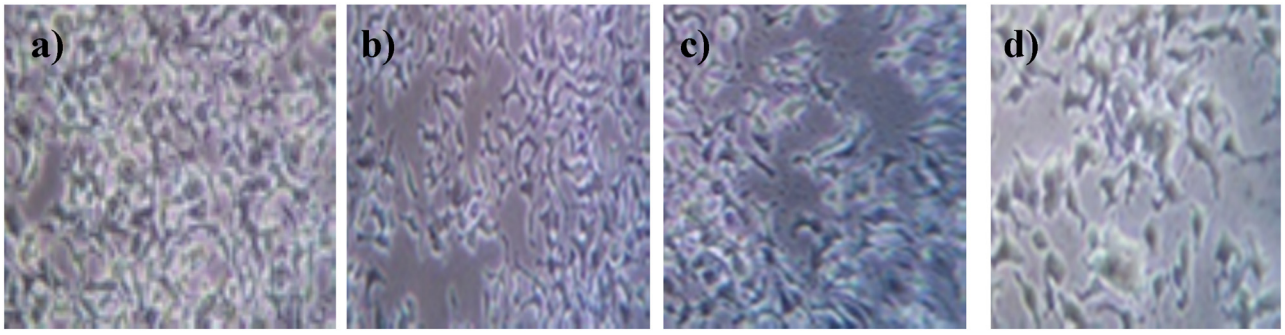

Figure 13: Anticancer activity of cancer cells. (a) Control Cell; (b) 25 µg/ml; (c) 100 µg/ml and (d) 500 µg/ml.

method and showed excellent activities in Gram-positive organisms compared to Gram-negative strains. 0.1 M CTAB + HAP had stronger antioxidant activity (79%). After 6 h, a high concentration (burst) of DOX-encapsulated HAP was released. According to drug release studies, controlling porosity aids in the prolonged and timed release of medications.

Acknowledgments: The authors extend their appreciation to the Deanship of Research and Graduate Studies at King Khalid University for funding this work through the Large Research Project under grant number RGP2/377/45. This work was supported by the National Research Foundation of Korea (NRF) grant funded by the Korean government (MSIT) (No.: NRF-2021R1F1A1062849).

Funding information: The authors extend their appreciation to the Deanship of Research and Graduate Studies at King Khalid University for funding this work through the Large Research Project under grant number RGP2/377/45.

Author contributions: Santhoshkumar Jayakodi: conceptualization, methodology, investigation, visualization, writing – original draft, and supervision. Rajeshkumar Shanmugam: conceptualization, methodology, investigation, and visualization. Elumalai Pandian: investigation and visualization. Mani Govindasamy: conceptualization and methodology. Jaber M. Asiri: conceptualization and methodology. Krishna Kumar Yadav: conceptualization and methodology. Jeong Ryeol Choi: editing, validation, and funding acquisition. All authors have accepted responsibility for the entire content of this manuscript and approved its submission.

Conflict of interest: The authors state no conflict of interest.

Data availability statement: The datasets generated during and/or analysed during the current study are available from the corresponding author on reasonable request.

References

[1] Li J, Zhang T, Liao Z, Wei Y, Hang R, Huang D. Engineered functional doped hydroxyapatite coating on titanium implants for osseointegration. J Mater Res Technol. 2023;27:122–52.

[2] Zhang B, Skelly JD, Maalouf JR, Ayers DC, Song J. Multifunctional scaffolds for facile implantation, spontaneous fixation, and accelerated long bone regeneration in rodents. Sci Transl Med. 2019;11(502):7411.

[3] Patel DK, Jin B, Dutta SD, Lim KT. Osteogenic potential of human mesenchymal stem cells on eggshells-derived hydroxyapatite nanoparticles for tissue engineering. J Biomed Mater Res Part B: Appl Biomater. 2020;108(5):1953–60.

[4] Sun XF, Ye Q, Jing Z, Li Y. Preparation of hemicellulose-g-poly (methacrylic acid)/carbon nanotube composite hydrogel and adsorption properties. Polym Compos. 2014;35(1):45–52.

[5] Zhou J, See CW, Sreenivasamurthy S, Zhu D. Customized additive manufacturing in bone scaffolds – the gateway to precise bone defect treatment. Research. 2023;6:0239.

[6] Do AV, Khorsand B, Geary SM, Salem AK. 3D printing of scaffolds for tissue regeneration applications. Adv Healthc Mater. 2015;4(12):1742–62.

[7] Alaribe FN, Manoto SL, Motaung SC. Scaffolds from biomaterials: advantages and limitations in bone and tissue engineering. Biologia. 2016;71(4):353–66.

[8] Kumar A, Han S-S. Efficacy of bacterial nanocellulose in hard tissue regeneration: a review. Materials. 2021;14(17):4777.

[9] Francis AP, Augustus AR, Chandramohan S, Bhat SA, Priya VV, Rajagopalan R. A review on biomaterials-based scaffold: an emerging tool for bone tissue engineering. Mater Today Commun. 2022;34:105124.

[10] Wang X, Fang J, Zhu W, Zhong C, Ye D, Zhu M, et al. Bioinspired highly anisotropic, ultrastrong and stiff, and osteoconductive mineralized wood hydrogel composites for bone repair. Adv Funct Mater. 2021;31(20):2010068.

[11] Su L-J, Zhang J-H, Gomez H, Murugan R, Hong X, Xu D, et al. Reactive oxygen species-induced lipid peroxidation in apoptosis, autophagy, and ferroptosis. Oxid Med Cell Longev. 2019;2019:5080843.

[12] Jampilek J, Placha D. Advances in use of nanomaterials for musculoskeletal regeneration. Pharmaceutics. 2021;13(12):1994.

[13] Jayakodi S, Shanmugam VK. Statistical optimization of copper oxide nanoparticles using response surface methodology and Box–Behnken design towards in vitro and in vivo toxicity assessment. Biointerface Res Appl Chem. 2021;11(3):10027–39.

[14] Chaudhary MR, Chaudhary S, Sharma Y, Singh TA, Mishra AK, Sharma S, et al. Aging, oxidative stress and degenerative diseases: mechanisms, complications and emerging therapeutic strategies. Biogerontology. 2023;24:1–54.

[15] Zieniewska I, Maciejczyk M, Zalewska A. The effect of selected dental materials used in conservative dentistry, endodontics, surgery, and orthodontics as well as during the periodontal treatment on the redox balance in the oral cavity. Int J Mol Sci. 2020;21(24):9684.

[16] Jayakodi S, Kim H, Menon S, Shanmugam VK, Choi I, Sekhar MR, et al. Preparation of novel nanoformulation to enhance efficacy in the treatment of cardiovascular disease. Biomimetics. 2022;7(4):189.

[17] Yin X, Chen K, Cheng H, Chen X, Feng S, Song Y, et al. Chemical stability of ascorbic acid integrated into commercial products: A review on bioactivity and delivery technology. Antioxidants. 2022;11(1):153.

[18] Panda S, Biswas CK, Paul S. A comprehensive review on the preparation and application of calcium hydroxyapatite: A special focus on atomic doping methods for bone tissue engineering. Ceram Int. 2021;47(20):28122–44.

[19] Shi H, Zhou Z, Li W, Fan Y, Li Z, Wei J. Hydroxyapatite based materials for bone tissue engineering: A brief and comprehensive introduction. Crystals. 2021;11(2):149.

[20] Du M, Chen J, Liu K, Xing H, Song C. Recent advances in biomedical engineering of nano-hydroxyapatite including dentistry, cancer treatment and bone repair. Compos Part B: Eng. 2021;215:108790.

[21] Wahid F, Huang L-H, Zhao X-Q, Li W-C, Wang Y-Y, Jia S-R, et al. Bacterial cellulose and its potential for biomedical applications. Biotechnol Adv. 2021;53:107856.

[22] Mohana S, Sumathi S. Synthesis of zinc oxide using Agaricus bisporus and its in-vitro biological activities. J Environ Chem Eng. 2020;8(5):104192.
[23] Imoisili PE, Ukoba KO, Jen T-C. Green technology extraction and characterisation of silica nanoparticles from palm kernel shell ash via sol–gel. J Mater Res Technol. 2020;9(1):307–13.
[24] Sriramulu M, Shukla D, Sumathi S. Aegle marmelos leaves extract mediated synthesis of zinc ferrite: antibacterial activity and drug delivery. Mater Res Express. 2018;5(11):115404.
[25] Imoisili PE, Jen T-C. Microwave-assisted sol–gel template-free synthesis and characterization of silica nanoparticles obtained from South African coal fly ash. Nanotechnol Rev. 2022;11(1):3042–52.
[26] Mohana S, Sumathi S. Agaricus bisporus mediated synthesis of cobalt ferrite, copper ferrite and zinc ferrite nanoparticles for hyperthermia treatment and drug delivery. J Clust Sci. 2023;35:1–14.
[27] Imoisili PE, Ukoba KO, Jen T-C. Synthesis and characterization of amorphous mesoporous silica from palm kernel shell ash. Bol Soc Esp Ceram Vidrio. 2020;59(4):159–64.
[28] Martínez-Castañón G, Loyola-Rodríguez J, Zavala-Alonso N, Hernández-Martínez S, Niño-Martínez N, Ortega-Zarzosa G, et al. Preparation and characterization of nanostructured powders of hydroxyapatite. Superficies Vacio. 2012;25(2):101–5.
[29] Kannan S, Lemos A, Ferreira J. Synthesis and mechanical performance of biological-like hydroxyapatites. Chem Mater. 2006;18(8):2181–6.
[30] Kuriakose TA, Kalkura SN, Palanichamy M, Arivuoli D, Dierks K, Bocelli G, et al. Synthesis of stoichiometric nano crystalline hydroxyapatite by ethanol-based sol–gel technique at low temperature. J Cryst Growth. 2004;263(1–4):517–23.
[31] Panda R, Hsieh M, Chung R, Chin T. FTIR, XRD, SEM and solid state NMR investigations of carbonate-containing hydroxyapatite nanoparticles synthesized by hydroxide-gel technique. J Phys Chem Solids. 2003;64(2):193–9.
[32] Yang H, Wang Y. Morphology control of hydroxyapatite microcrystals: Synergistic effects of citrate and CTAB. Mater Sci Eng. 2016;62:160–5.
[33] Ma J, Chen C, Wang D, Shi J. Textural and structural studies of sol–gel derived SiO_2–CaO–P_2O_5–MgO glasses by substitution of MgO for CaO. Mater Sci Eng. 2010;30(6):886–90.
[34] Barralet J, Best S, Bonfield W. Carbonate substitution in precipitated hydroxyapatite: an investigation into the effects of reaction temperature and bicarbonate ion concentration. J Biomed Mater Res. 1998;41(1):79–86.
[35] Anbalagan Balamurugan JM, Faure J, HichamBenhayoune L, Sockallingum G, Banchet V, Bouthors S, et al. Synthesis and structural analysis of sol–gel derived stoichiometric monophasic hydroxyapatite. Ceram-Silik. 2006;50(1):27–31.
[36] Fukuda J, Shinoda K. Coordination of water molecules with Na+ cations in a beryl channel as determined by polarized IR spectroscopy. Phys Chem Miner. 2008;35:347–57.
[37] Fan Z-W, Xiong Y-Q, Shao Y-J, Wen C-H. Textural and chemical characteristics of beryl from the Baishawo Be-Li-Nb-Ta pegmatite deposit, Jiangnan Orogen: Implication for rare metal pegmatite genesis. Ore Geol Rev. 2022;149:105094.
[38] Tank KP, Chudasama KS, Thaker VS, Joshi MJ. Cobalt-doped nanohydroxyapatite: synthesis, characterization, antimicrobial and hemolytic studies. J Nanopart Res. 2013;15:1–11.
[39] Chen L, Mccrate JM, Lee JC, Li H. The role of surface charge on the uptake and biocompatibility of hydroxyapatite nanoparticles with osteoblast cells. Nanotechnology. 2011;22(10):105708.
[40] Kumar R, Prakash K, Cheang P, Khor K. Temperature driven morphological changes of chemically precipitated hydroxyapatite nanoparticles. Langmuir. 2004;20(13):5196–200.
[41] Gulcin İ. Antioxidants and antioxidant methods: An updated overview. Arch Toxicol. 2020;94(3):651–715.
[42] Vinayagam R, Kandati S, Murugesan G, Goveas LC, Baliga A, Pai S, et al. Bioinspiration synthesis of hydroxyapatite nanoparticles using eggshells as a calcium source: Evaluation of Congo red dye adsorption potential. J Mater Res Technol. 2023;22:169–80.
[43] Sánchez-Campos D, Mendoza-Anaya D, Reyes-Valderrama M, Esteban-Gómez S, Rodríguez-Lugo V. Cationic surfactant at high pH in microwave HAp synthesis. Mater Lett. 2020;265:127416.
[44] Singh G, Jolly SS, Singh RP. Investigation of surfactant role in synthesis of hydroxyapatite nanorods under microwave and hydrothermal conditions. Mater Today: Proc. 2020;26:2701–10.
[45] Sierra L, Valange S, Barrault J, Guth J-L. Templating behavior of a triblock copolymer surfactant with very long hydrophilic PEO chains (PEO140PPO39PEO140) for the synthesis of cubic mesoporous silica with large cage-like cavities. Microporous Mesoporous Mater. 2008;113(1–3):352–61.
[46] Yan L, Xu Z, Wang X. Synergistic effects of organically modified montmorillonite on the flame-retardant and smoke suppression properties of transparent intumescent fire-retardant coatings. Prog Org Coat. 2018;122:107–18.
[47] Zhu Z, Wang Aj, Xue H, Liu R, Miao L, Liu Dj, et al. Effect of cetyltrimethyl-ammonium bromide on the properties of hydroxyapatite nanoparticles stabilized Pickering emulsion and its cured poly (L-lactic acid) materials. J Biomed Mater Res Part B: Appl Biomater. 2021;109(10):1552–62.
[48] Yan HC, Li QX, Geng T, Jiang YJ. Properties of the quaternary ammonium salts with novel counterions. J Surfactants Deterg. 2012;15:593–9.
[49] Sotler R, Poljšak B, Dahmane R, Jukić T, Pavan Jukić D, Rotim C, et al. Prooxidant activities of antioxidants and their impact on health. Acta Clin Croat. 2019;58(4):726–36.
[50] Vijayalakshmi U. A systematic review of the interaction and effects generated by antimicrobial metallic substituents in bone tissue engineering. Metallomics. 2020;12(10):1458–79.
[51] De Lama-Odría MD, Del Valle LJ, Puiggalí J. Hydroxyapatite biobased materials for treatment and diagnosis of cancer. Int J Mol Sci. 2022;23(19):11352.
[52] Aziz MA, Diab AS, Mohammed AA. Antioxidant categories and mode of action. Antioxidants. 2019;2019:3–22.
[53] Vishnoi H, Bodla RB, Kant R, Bodla R. Green tea (Camellia sinensis) and its antioxidant property: a review. Int J Pharm Sci Res. 2018;9(5):1723–36.
[54] Munteanu IG, Apetrei C. Analytical methods used in determining antioxidant activity: A review. Int J Mol Sci. 2021;22(7):3380.
[55] Lara-Ochoa S, Ortega-Lara W, Guerrero-Beltrán CE. Hydroxyapatite nanoparticles in drug delivery: physicochemistry and applications. Pharmaceutics. 2021;13(10):1642.
[56] Xihua Z, Changxia L, Musen L, Yunqiang B, Junlong S. Fabrication of hydroxyapatite/diopside/alumina composites by hot-press sintering process. Ceram Int. 2009;35(5):1969–73.
[57] Predoi SA, Ciobanu CS, Motelica-Heino M, Chifiriuc MC, Badea ML, Iconaru SL. Preparation of porous hydroxyapatite using cetyl trimethyl ammonium bromide as surfactant for the removal of lead ions from aquatic solutions. Polymers. 2021;13(10):1617.